

Shock propagation in a driven hard sphere gas: molecular dynamics simulations and hydrodynamics

Amit Kumar^{1,2,*} and R. Rajesh^{1,2,†}

¹*The Institute of Mathematical Sciences, C.I.T. Campus, Taramani, Chennai 600113, India*

²*Homi Bhabha National Institute, Training School Complex, Anushakti Nagar, Mumbai 400094, India*

(Dated: September 19, 2024)

The continuous injection of energy at a localized region in space in a stationary gas creates a shock wave that propagates radially outwards. We study the hydrodynamics of this disturbance using event driven molecular dynamics of a hard sphere gas in three dimensions, the numerical solution of the Euler equation with a virial equation of state for the gas, and the numerical solution of the Navier-Stokes equation. We show that the results from the Euler equation do not agree with the data from hard sphere simulations. Including dissipative terms through the Navier-Stokes equation results in reasonably good description of the data, when the coefficients of dissipation are chose parametrically.

I. INTRODUCTION

The study of shock propagation following an intense explosion is a classic problem in gas dynamics [1–3]. In the initial transient phase, the system emits energy through radiation. However, as the system cools down, it transitions into the hydrodynamic phase, where the primary means of energy transport are the movements of particles, and the significance of radiation diminishes. The disturbance grows radially outward with a shock front separating the affected region from the ambient region. Across this front, the thermodynamic quantities like density, velocity, temperature, and pressure change abruptly, and the magnitude of these discontinuities is determined by the Rankine-Hugoniot boundary conditions [1–3]. Straightforward dimensional analysis reveals that the radius, $R(t)$, of the shock front exhibits a power-law growth with respect to time t as $R(t) \sim (E_i t^2 / \rho_0)^{1/(d+2)}$ in d -dimensions, where E_i and ρ_0 are the initial input energy and ambient mass density of the gas [1, 4–10]. The power-law exponent has been confirmed in the Trinity explosion [4, 5], and in blast waves produced by the deposition of laser pulses in gas jets [11], plasma [12], and atomic clusters of different gases [13].

Beyond the power-law growth of $R(t)$, it is also feasible to obtain the spatio-temporal behavior of density, velocity, temperature, and pressure. These are governed by the continuity equations for mass, momentum, and the energy. In the scaling limit, dissipation factors such as heat conduction and viscosity become negligible, and the hydrodynamics is governed by the Euler equation. For an ideal gas, within the assumption of local equilibrium, Taylor, von-Neumann, and Sedov obtained the exact solution of scaling functions for density, velocity, temperature, and pressure [4–8]. We refer to this self-similar solution as the TvNS solution. Only recently has the validity

of the TvNS theory been checked in simulations of hard spheres in three [14–16], two [14, 16–18] and one dimensions [19, 20]. It was found that the event driven molecular dynamics (EDMD) simulations in two and three dimensions found significant differences between the TvNS theory and simulations near the shock center and quantified through the exponents governing the power law behavior of the different scaling functions [15–17]. It was shown that when dissipation terms are included in the Euler equation giving rise to the Navier-Stokes equation, then the discrepancies of the theory with simulations can be accounted for both in one dimension [19, 20] as well as higher dimensions [16]. The crossover behavior of the scaling functions from the Euler solution to the Navier-Stokes solution near the shock center has been quantified in one [19, 20] and two dimensions [21]. This resolution shows that the order of taking the limits – first taking the scaling limit and then finding the solution, or finding the solution of the Navier-Stokes equation and then taking the scaling limit – matter for the final answer. In particular, the boundary conditions satisfied near the shock center are different for the two cases.

A closely related problem is that of shocks that are generated when there is a continuous input of energy at one point in space. Now, unlike the problem of single impact discussed above, the system is now driven away from equilibrium due to the constant energy current. This problem has relevance for the study of the motion of interstellar gas due to the effect continuous energy injection by the stellar wind [22, 23]. Let the source be such that energy increases as $E(t) = E_0 t^\delta$, where E_0 and δ are positive constants. From dimensional analysis, one obtains that the radius of shock front grows as $R(t) \sim (E_0 / \rho_0)^{\frac{1}{\delta+2}} t^{\frac{2+\delta}{\delta+2}}$, in d -dimensions. The TvNS solution for the single impact can now be generalized to $\delta \neq 0$. The exact solution for the different thermodynamic quantities for an ideal gas, within the Euler equation, was found by Dokuchaev in three dimensions [9].

In this paper, we focus on the hydrodynamics of the shocks in the presence of an energy source. Given that the description of the shock due to a single impact re-

* kamit@imsc.res.in

† rrajesh@imsc.res.in

quired dissipation terms, it is highly likely that the driven shocks also are not described by the Euler equation or equivalently the Dokuchaev solution. In addition, it is not clear whether the Navier-Stokes equation can describe the different thermodynamic quantities for the driven shock, given that the system is far from equilibrium. To address these issues, we study the problem using different approaches. Using large scale EDMD simulations of a hard sphere gas in which particles near the origin are given energy continuously, we obtain the scaling behavior of the radius of the shock front, and the density, velocity, pressure and temperature fields. We show that these data are very different from the solution of the Euler equation for the ideal gas. We then show that including steric effects by using a virial equation of state in the Euler equation does not resolve the discrepancy with EDMD data. We then develop a direct numerical solution (DNS) of the Navier-Stokes equation with energy input continuously near the origin and virial equation of state with 10 terms. We find that by choosing the heat conduction and viscosity parameter suitably, we are able to nearly match the EDMD data. The velocity field was not fully reproducible while the other fields are better reproduced. Also, near the shock center, there is some discrepancy but probably due to the different driving schemes used in the EDMD and DNS. We conclude that the description of the driven shocks requires the full Navier-Stokes equation. However, the match with the numerical data is not as good as the case of single impact.

The remainder of the paper is organized as follows. In Sec. II, we review the exact solution of Euler equation for driven shocks in an ideal gas, and find the asymptotic behavior of different scaling functions. In Sec. III A we numerically study the driven shock in a hard sphere gas using EDMD simulations. We verify the correctness of the simulations by benchmarking known behavior of physical quantities, and then show that the different scaling functions do not compare well with the exact solution. In Sec. III B, we modify the equation of state from ideal to virial equation of state to account for steric effects. We then numerically solve the Euler equation and quantify the effect of excluded volume on the solution. We also show that including steric effects do not resolve the discrepancy with EDMD data. In Sec. III C, we provide the numerical solution of the Navier-Stokes equation for virial equation of state, and do a parametric study to understand the effect of the dissipation terms on the scaling functions. In Sec. IV, we compare all the results obtained from the theory, EDMD, and DNS of NSE for hard sphere gas. We conclude with a summary and discussion in Sec. V.

II. REVIEW OF EULER EQUATION FOR DRIVEN SHOCK

In this section, we summarize the Euler equation describing the macroscopic dynamics of a driven shock. Consider a gas at rest having uniform density ρ_0 , and hence zero pressure and zero temperature everywhere. Energy is isotropically and continuously injected at one point (taken to be the origin) such that the total energy increases with time t as $E(t) = E_0 t^\delta$, $\delta \geq 0$. The driving generates a spherically symmetric shock which expands self similarly in time into the ambient gas. We define the shock front as the surface of discontinuity which separates the moving gas from the ambient stationary gas. A shock is said to be strong if $p_1/\rho_1 \gg p_0/\rho_0$, where p is the pressure, ρ is the mass density, and subscripts 1 and 0 indicate the quantities just behind and front of the shock respectively. Since $p_0 = 0$ for an initial stationary gas, the shock is always strong.

The scaling of the radius of shock front, $R(t)$, with time t , is uniquely determined by dimensional analysis [1, 7, 10], and in three dimensions is

$$R(t) \sim \left(\frac{E_0}{\rho_0}\right)^{1/5} t^{(2+\delta)/5}. \quad (1)$$

The macroscopic state of the gas at time t and position \vec{r} is described in terms of the following fields: density $\rho(\vec{r}, t)$, velocity $\vec{v}(\vec{r}, t)$, temperature $T(\vec{r}, t)$, and pressure $p(\vec{r}, t)$. Due to the spherical symmetry, the thermodynamic quantities depend only on radial distance r , and the velocity is radial,

$$\vec{v}(\vec{r}, t) = v(r, t)\hat{r}. \quad (2)$$

The continuity equations of locally conserved quantities, mass, momentum, and the energy, give the evolution of the fields. In the scaling limit, $r \rightarrow \infty$, $t \rightarrow \infty$, such that $rt^{-(2+\delta)/5}$ remains constant, the contribution of heat conduction and viscosity become negligible and the hydrodynamics is governed by the Euler equation. The continuity equations for mass, momentum and energy along radial direction for driven shock in 3-dimensional spherical polar coordinates is given by [1-3, 7, 9]

$$\partial_t \rho + \partial_r(\rho v) + \frac{2\rho v}{r} = 0, \quad (3)$$

$$\partial_t v + v \partial_r v + \frac{1}{\rho} \partial_r p = 0, \quad (4)$$

$$v \left(\epsilon + \frac{p}{\rho} + \frac{v^2}{2} \right) = \frac{U r}{R(t)} \left(\epsilon + \frac{v^2}{2} \right), \quad (5)$$

where $U = \dot{R}(t)$ is the speed of the shock front, and ϵ is the internal energy per unit volume of the gas. The integral form of the continuity equation for energy in Eq. (5) is obtained from the differential form by integrating over a tiny shell in radial direction. We refer to Ref. [9] for the derivation. For a gas, $\epsilon = T/(\gamma - 1)$, where γ is the adiabatic constant.

Assuming local thermal equilibrium, the local pressure p is related to the local temperature T and local density ρ through an equation of state (EOS), reducing the number of variables by one. A general EOS can be written as

$$p = k_B \rho T \mathbb{Z}(\rho), \quad (6)$$

where $\mathbb{Z}(\rho)$ is known as the compressibility factor of the EOS.

Across the shock front these thermodynamic quantities become discontinuous. The values of these quantities ahead and behind the shock front are related by the Rankine-Hugoniot boundary conditions [1, 3]:

$$\rho_1 = \left[1 + \frac{2}{(\gamma - 1)\mathbb{Z}(\rho_1)} \right] \rho_0, \quad (7)$$

$$v_1 = \frac{2U}{2 + (\gamma - 1)\mathbb{Z}(\rho_1)}, \quad (8)$$

$$p_1 = \frac{2\rho_0 U^2}{2 + (\gamma - 1)\mathbb{Z}(\rho_1)}. \quad (9)$$

$\gamma = 5/3$ is the adiabatic constant for mono-atomic gas in 3-dimensions.

It should also be noted that total energy $E(t)$ of the gas at time t should be equal to $E_0 t^\delta$, i.e.

$$E_0 t^\delta = \int_0^{R(t)} \left(\frac{\rho v^2}{2} + \frac{\rho T}{\gamma - 1} \right) 4\pi r^2 dr. \quad (10)$$

The continuity equations (3)–(5) are first order partial differential equations in both time and distance. These equations can be converted into ordinary differential equations using self similar solutions. We define dimensionless distance ξ and non-dimensionalised scaling functions $\tilde{R}, \tilde{u}, \tilde{T}, \tilde{P}$ corresponding to density ρ , velocity u , temperature T , and pressure p respectively as

$$\xi = r \left(\frac{E_0}{\rho_0} \right)^{-1/5} t^{-(2+\delta)/5}, \quad (11)$$

$$\rho(r, t) = \rho_0 \tilde{R}(\xi), \quad (12)$$

$$v(r, t) = \frac{r}{t} \tilde{u}(\xi), \quad (13)$$

$$T(r, t) = \frac{r^2}{t^2} \tilde{T}(\xi), \quad (14)$$

$$p(r, t) = \frac{\rho_0 r^2}{t^2} \tilde{P}(\xi). \quad (15)$$

We now specialize the solution to the ideal gas for which an exact solution may be found. For ideal gas $\mathbb{Z}(\rho) = 1$, and the equation of state (Eq. (6)) implies that,

$$\tilde{P} = \tilde{R}\tilde{T}. \quad (16)$$

The continuity equations, in terms of the scaling func-

tions, reduce to

$$(\alpha - \tilde{u}) \frac{d \log \tilde{R}}{d \log \xi} - \frac{d \tilde{u}}{d \log \xi} = 3\tilde{u}, \quad (17)$$

$$(\tilde{u} - \alpha) \frac{d \tilde{u}}{d \log \xi} + \tilde{T} \frac{d \log \tilde{R}}{d \log \xi} + \frac{d \tilde{T}}{d \log \xi} + \tilde{u}[\tilde{u} - 1] + 2\tilde{T} = 0, \quad (18)$$

$$\tilde{T} = \frac{\tilde{u}^2(\alpha - \tilde{u})(\gamma - 1)}{2(\gamma\tilde{u} - \alpha)}, \quad (19)$$

where $\alpha = (2 + \delta)/5$, while the Rankine-Hugoniot boundary conditions reduce to,

$$\tilde{R}(\xi = \xi_f) = \frac{\gamma + 1}{\gamma - 1}, \quad (20)$$

$$\tilde{u}(\xi = \xi_f) = \frac{2\alpha}{\gamma + 1}, \quad (21)$$

$$\tilde{T}(\xi = \xi_f) = \frac{2\alpha^2(\gamma - 1)}{(\gamma + 1)^2}. \quad (22)$$

Given the boundary conditions (20)–(22) at ξ_f , the differential equations (17)–(19) may be integrated to obtain the scaling functions. However, ξ_f remains indeterminate. The value of ξ_f is uniquely fixed from the non-dimensionalised form of Eq. (10),

$$4\pi \int_0^{\xi_f} \left(\frac{\tilde{R}\tilde{u}^2}{2} + \frac{\tilde{R}\tilde{T}}{\gamma - 1} \right) \xi^4 d\xi = 1. \quad (23)$$

An analytical solution of Eqs (17)–(19) with boundary conditions given in Eqs. (20)–(22) is possible [9]. For the completeness of the results, we summarize the derivation in Appendix A.

From the exact solution, the behavior of the thermodynamic quantities near the shock center ($\xi \rightarrow 0$) may be derived. These results will be useful for comparison with results from particle based simulations. We find that when $\xi \rightarrow 0$, then $\tilde{u} \rightarrow \frac{\alpha}{\gamma}$. The asymptotic behavior of $\tilde{R}, \tilde{u}, \tilde{T}$, and \tilde{P} near $\xi \rightarrow 0$ are,

$$\tilde{u} - \frac{\alpha}{\gamma} \sim \xi^{\frac{2\gamma+1}{\gamma-1}} \quad (24)$$

$$\tilde{R} \sim \xi^{\frac{3}{\gamma-1}} \quad (25)$$

$$\tilde{T} \sim \xi^{-\frac{2\gamma+1}{\gamma-1}}, \quad (26)$$

$$\tilde{P} \sim \xi^{-2}. \quad (27)$$

The exponents of the different non-dimensionalised thermodynamic quantities only depend on γ , and are independent of δ , while the exponent of \tilde{P} is a constant. Since the exponents are independent of δ , the power laws are as for the case for shocks arising from a single impact [15].

We check for the correctness of the asymptotic analysis for $\xi \rightarrow 0$ by comparing them with the full exact solutions in Fig. 1 where the non-dimensionalised functions

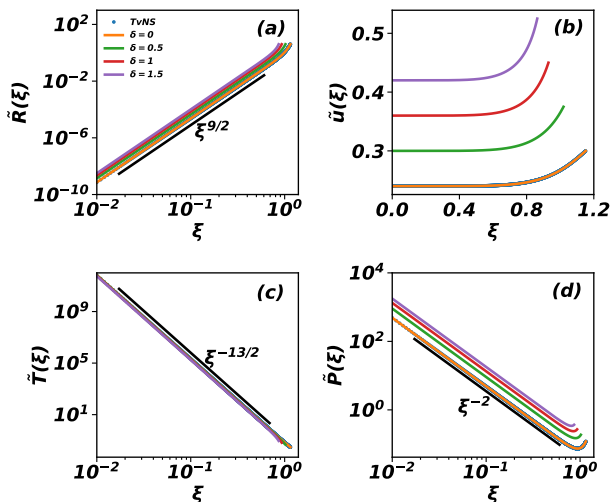


FIG. 1. The exact solutions of the continuity equations (17)–(19) for the non-dimensionalised (a) density, \tilde{R} , (b) velocity, \tilde{u} , (c) temperature, \tilde{T} , and (d) pressure, \tilde{P} are compared with the asymptotic behavior when $\xi \rightarrow 0$ (see Eqs. (24)–(27)). The data are for four different values of $\delta = 0, 0.5, 1, 1.5$. The label *TvNS* refers to the solution of Euler equation with ideal EOS for a single impact.

obtained from exact solution of Euler Eqs. (17)–(19) are shown for four different values of $\delta = 0, 0.5, 1, 1.5$. It is clear that the power laws followed by different thermodynamic quantities are independent of δ , and their exponents are consistent with Eqs. (24)–(27). Also, we note that the exact solution with $\delta = 0$ reproduces the TvNS solution.

III. RESULTS

A. Comparison of exact results of Euler equation for ideal gas with EDMD Simulations

In this section we compare the exact solution of the Euler equation for the thermodynamic quantities (see Sec. II) with results from EDMD simulations of a particle based model. The simulation results are for $\delta = 1$ when energy is input at a constant rate, i.e., $E(t) = E_0 t$.

We first describe the model. Consider a system of N identical hard spheres, labeled $1, 2, \dots, N$, distributed uniformly in space. The particles are initially at rest. Energy is input at a constant rate at the origin, and the system evolves in time through momentum and energy conserving binary collisions between particles. All masses and distances are measured in terms of the particle mass m and diameter D , hence we set the mass and diameter of each particle to 1. Time is measured in terms of the inherent time scale $(mD^2/E_0)^{1/3}$.

In a binary collision, the normal component of the relative velocity is reversed while the tangential component remains unchanged. If \vec{v}_i, \vec{v}_j are the pre-collision veloc-

ities of colliding particles i, j , then their post-collision velocities \vec{v}'_i, \vec{v}'_j are given by

$$\vec{v}'_i = \vec{v}_i - (\hat{n} \cdot \vec{v}_{ij}) \hat{n}, \quad (28)$$

$$\vec{v}'_j = \vec{v}_j - (\hat{n} \cdot \vec{v}_{ji}) \hat{n}, \quad (29)$$

where \hat{n} is the unit vector along the line joining the centers of the two particles at the time of contact, and $\vec{v}_{ij} = \vec{v}_i - \vec{v}_j$ is their relative velocity.

We model the continuous driving as follows. Consider a sphere of radius R_0 centered about the origin or equivalently center of the simulation box. In each time interval Δt , a particle within the sphere of radius R_0 is chosen at random and its velocity is modified to

$$\vec{v}'_i = \vec{v}_i + \vec{\eta}, \quad (30)$$

where the components of the noise $\vec{\eta}$ are drawn from a uniform distribution between $-\sqrt{2E_0\Delta t}$ to $\sqrt{2E_0\Delta t}$. For such a driving it is straightforward to show that total energy increases as

$$E(t) = E_0 t. \quad (31)$$

The simulations are done using the event driven molecular dynamics scheme where the system evolves from event to event, the events being collisions, driving and cell crossing [24]. Boundary effects are avoided by choosing the number of particles and box size such that the shock does not reach the boundary within the simulation time. The EDMD simulations were performed for $N = 4 \times 10^7$ particles with mass density $\rho_0 = 0.4013$, $E_0 = 2.5 \times 10^{-6}$, and $R_0 = 15.0$.

We measure the radial density, velocity, temperature, and pressure in our simulation. We define density $\rho(\vec{r}, t)$ and velocity $v(\vec{r}, t)$ as local average of density and radial velocity at position \vec{r} and time t . Local temperature $T(\vec{r}, t)$ is defined as the variance of local velocity. We measure local pressure for 3-dimensional hard spheres [25] as

$$p = \rho T - \frac{\rho}{3N'\Delta t'} \sum_{\text{collisions}} \vec{r}_{ij} \cdot \vec{v}_{ij}, \quad (32)$$

where $\vec{r}_{ij} = \vec{r}_i - \vec{r}_j$ is the distance between the colliding sphere, $\Delta t'$ and N' are time interval and average number of particles belonging to a particular radial bin in which pressure is being measured.

The isotropic driving generates a spherically symmetric shock which grows radially outwards. To visualize the growing shock, in Fig. 2, we plot the x - and y - coordinates of all the particles lying between the planes $z = -1$ and $z = 1$. It can be observed that there is a sharp boundary between the moving particles (red) and the stationary particles (green), and the shock front expands in time. Also, the density near the shock center is close to zero.

We first confirm that with the simulation scheme, the total energy increases as $E_0 t$ as can be seen from Fig. 3(a). To further benchmark our simulations, we

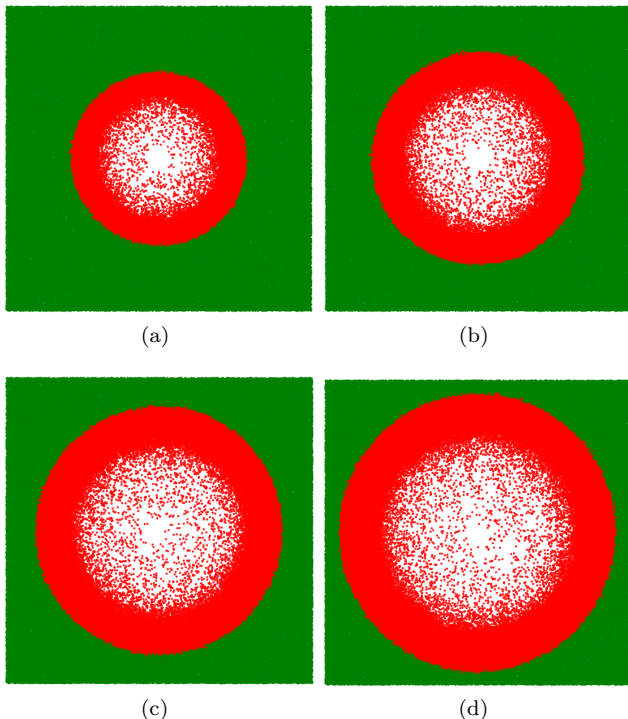


FIG. 2. Snapshots of a cross-section of shock in the x - y plane obtained by plotting the coordinates of only the particles with z -coordinates between -1 to 1 . The data are for the times (a) $t = 1357$, (b) $t = 1900$, (c) $t = 2443$, (d) $t = 2986$. Stationary particles are colored green while moving particles are colored red. The data shown here are for ambient gas density $\rho_0 = 0.4013$ and 2×10^7 number of particles.

compare the power law growth of the radius of the shock and the radial momentum with time with known scaling laws. For the driven shock with $\delta = 1$, in the scaling regime, the total radial momentum $M(t)$, and the radius of shock front $R(t)$ should increase with time as

$$M(t) \sim t^{7/5}, \quad (33)$$

$$R(t) \sim t^{3/5}. \quad (34)$$

The simulation results reproduce these power laws for large time, as can be seen in Fig. 3(b) and (c). $R(t)$ is measured as the mean value of the radial distance of the moving particles, while $M(t)$ is obtained as the cumulative radial velocity. For short times, there is a deviation from these power laws. This is due to the radius of the shock being comparable to the driving scale R_0 . The crossover time also gives us a measure of the time beyond which the scaling regime is reached.

We now compare the predictions for the different thermodynamic quantities as obtained from Euler equation with ideal EOS with the results from EDMD, as shown in Fig. 4. The EDMD data for four different times collapse onto one curve when scaled appropriately, thus validating the scaling in Eqs. (11)–(15). However, the EDMD simulation results do not match with the exact solution

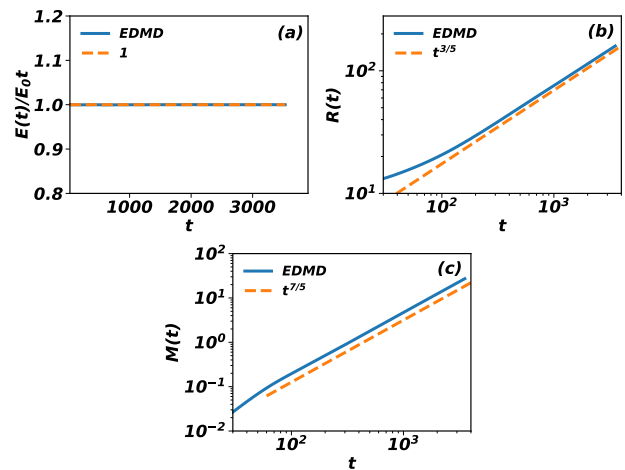


FIG. 3. Power law growth of (a) total energy $E(t) = E_0 t$, (b) radius of the shock front $R(t) \sim t^{3/5}$, and (c) total radial momentum $M(t) \sim t^{7/5}$ of the system. Solid lines represent the results from EDMD, and dashed lines represent the respective power laws.

for any value of ξ . This is most easily seen for \tilde{R} [see Fig. 4(a)] and \tilde{u} [see Fig. 4(b)], where the exact results, shown by dotted lines' do not overlap with the numerical data anywhere. The scaling function \tilde{T} varies as ξ^{-2} in EDMD for $\xi \rightarrow 0$ while it behaves as $\xi^{-13/2}$ in the exact solution [see Fig. 4(c)]. The scaling function \tilde{P} has nearly the same power law for $\xi \rightarrow 0$. We also note that the position of the shock front is different for the exact solution and the simulation data. We have checked that the position of the shock front is not dependent on R_0 , the driving region.

We now explore whether the discrepancy between simulation data and the results from Euler equation with ideal gas equation of state can be explained in terms of including the excluded volume effects of the hard sphere gas into the Euler equation.

B. Comparison of solution of Euler equation for hard sphere EOS with EDMD Simulations

In a hard sphere gas, steric effects are important unlike in ideal gas. Thus, a more realistic EOS is needed to account for these effects. Virial EOS is the most common EOS for hard spheres, which take the following form,

$$p = \rho k_B T \left(1 + \sum_{i=2}^{\infty} B_i \rho^{i-1} \right), \quad (35)$$

with compressibility factor,

$$\mathbb{Z}(\rho) = 1 + \sum_{i=2}^{\infty} B_i \rho^{i-1}. \quad (36)$$

where B_i denotes the i^{th} virial coefficient. We tabulate the known values of the virial coefficients [26] in Table I.

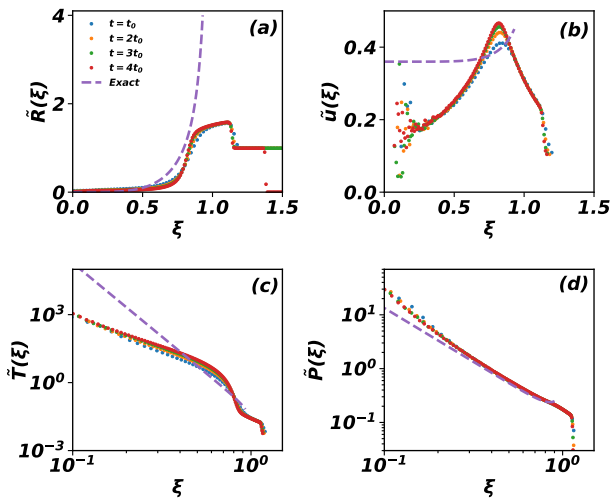


FIG. 4. Comparison of the results from Euler equation with EDMD for the different thermodynamic quantities: (a) density \tilde{R} , (b) velocity \tilde{u} , (c) temperature \tilde{T} , and (d) pressure \tilde{P} . The symbols represent the profiles obtained from EDMD at four different times, where $t_0 = 1357$, and the dashed lines represent the exact solution of Euler Eqs. (17)–(19). The collapse of the data for different times onto one curve shows that system has reached to scaling regime. The data for EDMD shown here are ambient gas density $\rho_0 = 0.4013$.

TABLE I. The numerical values of the virial coefficients B_i for a three dimensional hard sphere gas of particles of diameter one. The data are taken from Ref. [26].

i	B_i
2	$\frac{2\pi}{3}$
3	$\frac{5}{8}B_2^2$
4	$\left[\frac{2707}{4480} + \frac{219\sqrt{2}}{2240\pi} - \frac{4131}{4480} \frac{\arccos[1/3]}{\pi} \right] B_2^3$
5	$0.110252B_2^4$
6	$0.03888198B_2^5$
7	$0.01302354B_2^6$
8	$0.0041832B_2^7$
9	$0.0013094B_2^8$
10	$0.0004035B_2^9$

For hard core gases B_i , does not depend on temperature and is therefore only depends on the shape of the particles.

The Euler Eqs. (3)–(5) with the hard sphere gas EOS

TABLE II. The numerical values of ξ_f for the hard sphere gas when virial EOS truncated at the i -th term, in three dimensions. The data for ξ_f for TvNS solution in three dimensions is taken from Ref. [15]. These data are for hard sphere gas with diameter one, $\gamma = 5/3$, density 0.4013.

i	$\xi_f(TvNS)$	$\xi_f(\delta = 0.5)$	$\xi_f(\delta = 1.0)$
2	1.361	1.206925	1.101329
4	1.499	1.328129	1.211471
6	1.521	1.346806	1.228195
8	1.524	1.349511	1.230584
10	1.524	1.349894	1.230918

can be simplified in terms of scaling functions as

$$(\alpha - \tilde{u}) \frac{d \log \tilde{R}}{d \log \xi} - \frac{d \tilde{u}}{d \log \xi} = 3 \tilde{u}, \quad (37)$$

$$(\tilde{u} - \alpha) \xi \frac{dV}{d\xi} + \frac{d(\tilde{T}\mathbb{Z})}{d \log \xi} + \tilde{T}\mathbb{Z} \left(\frac{d \log \tilde{R}}{d \log \xi} + 2 \right) + \tilde{u}^2 - \tilde{u} = 0, \quad (38)$$

$$\tilde{T} = \frac{\tilde{u}^2(\alpha - \tilde{u})(\gamma - 1)}{2[(\gamma - 1)\tilde{u}\mathbb{Z} - (\alpha - \tilde{u})]}. \quad (39)$$

The Rankine-Hugoniot boundary conditions, Eqs. (7)–(9), for the hard sphere gas in terms of scaling functions reduce to

$$\tilde{R}(\xi_f) = 1 + \frac{2}{(\gamma - 1)\mathbb{Z}}, \quad (40)$$

$$\tilde{u}(\xi_f) = \frac{2\alpha}{2 + (\gamma - 1)\mathbb{Z}}, \quad (41)$$

$$\tilde{T}(\xi_f) = \frac{2\alpha^2(\gamma - 1)}{[2 + (\gamma - 1)\mathbb{Z}]^2}. \quad (42)$$

The ordinary differential equations (37)–(39) with the boundary conditions, Eqs. (40)–(42) can be solved numerically. As for the ideal gas, we find the value of ξ_f recursively by satisfying the energy constraint Eq. (23).

We obtain the numerical solution of Euler Eqs. (39)–(37) for hard sphere gas with ambient density $\rho_0 = 0.4013$, for different values of δ , with virial EOS truncated at different terms. From the numerical solution, we calculated the values of ξ_f when virial EOS truncated at various terms. These values are tabulated in Table II. We find that ξ_f does not change much between the equation of state truncated at the 8-th and 10-th virial terms for both values of δ .

We now examine the role of the truncation of the equation of state on the thermodynamics quantities. Figure 5 shows the variation of the scaling functions \tilde{R} , \tilde{u} , \tilde{T} , and \tilde{P} with ξ for hard spheres for $\delta = 1$, when the virial EOS is truncated at $i = 0, 2, 4, 6, 8, 10$ -th terms. We find that including the virial terms does affect the thermodynamic quantities, especially density and velocity. However, the data corresponding to $i = 8, 10$ lie on top of each other

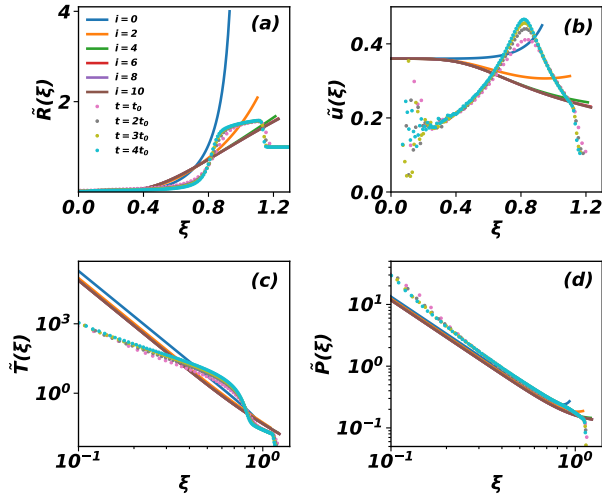


FIG. 5. Non-dimensionalised thermodynamic quantities obtained by numerically solving Euler equation (lines) with virial equation of state (see Eqs. (39)–(37)) for $\delta = 1$ when the virial EOS is truncated at $i = 0, 2, 4, 6, 8$, and 10^{th} term, and the EDMD simulations data (dots) for four different times. The curves corresponding to $i = 8, 10$ collapse on each other showing negligible truncation error at $i = 10$. $i = 0$ represents the ideal EOS. The data are for ambient gas density $\rho_0 = 0.4013$.

showing negligible truncation error at $i = 10$. Thus, truncating virial EOS at $i = 10$ is a good approximation to the actual EOS. We also point out that the exponents characterizing the power-law behavior do not depend on the truncation.

We now examine the role of δ , the driving rate, on the thermodynamic quantities, within the Euler equation. For this, we keep the truncation of the virial expansion fixed at $i = 10$ and vary δ . We find that the exponents characterizing the power law behavior of the different thermodynamic quantities are independent of δ (see Fig. 6), and hence same as that for the single impact with ideal gas EOS.

Finally, we note that including the hard-core effects into the Euler equation does not resolve the discrepancy between EDMD simulations and hydrodynamics based on Euler equation. This can be seen from Fig. 5 for $\delta = 1$. We see that the position of shock front from numerical solution, although it has come little closer to EDMD now, still falls at the different point than the EDMD, however the values of scaling functions at the shock fronts are same in the two. From this comparison, we again find that the EDMD results do not match, neither qualitatively nor quantitatively, with the numerical solution of Euler equation for hard sphere gas through the range of ξ . Therefore, the equation of state is not reason of the mismatch. Hence, the reason of the mismatch still remains a question.

The qualitative behavior of scaling functions for hard

sphere gas, obtained from the numerical solution of Euler equation, are exactly same as the exact solution for ideal

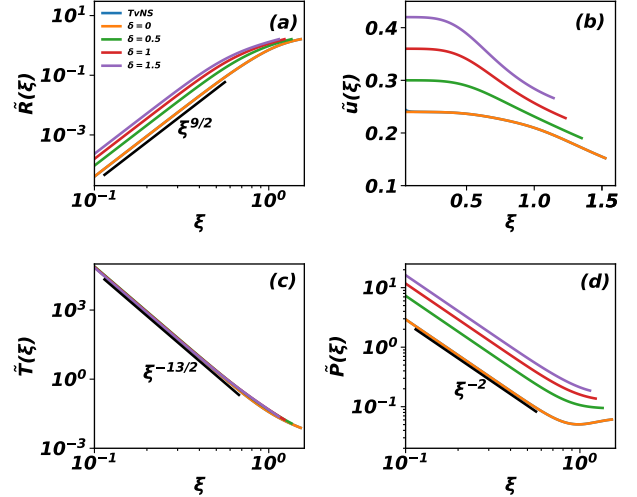


FIG. 6. Power law behavior of scaling functions obtained from numerical solution of Euler equation for hard spheres (see Eqs. (39)–(37)) for four different values of $\delta = 0, 0.5, 1, 1.5$. From the plot, power law behaviors of different scaling functions seem to be independent of the value of δ and are the same as in the ideal gas case. The data shown here are for ambient gas density $\rho_0 = 0.4013$, and for the virial EOS truncated at $i = 10$.

gas. In fact, the variation $\tilde{T} \rightarrow \xi^{-2}$, in EDMD, indicates that $T(r, t) \rightarrow r^0 t^{-4/5}$ close to the shock center, which means that the temperature $T(r, t)$ decreases in time and the slope with respect radial distance r is zero, while the behavior $\tilde{T} \rightarrow \xi^{-13/2}$ in numerical solution shows that the temperature $T(r, t)$ varies as $r^{-9/2} t^{19/10}$ which gives divergent spatial slope of temperature at the shock center. The divergent temperature leads to infinite energy in the system, which is unphysical for a finitely driven system. Since the heat conduction term put a boundary condition: $\vec{\nabla} T = 0$, so the solution of full Navier-Stokes equation may resolve the discrepancy between EDMD and hydrodynamics.

C. Navier-Stokes equation

In Euler equation, it was assumed that at long time, the contribution of the dissipation terms (heat conduction and viscosity) become negligible in the scaling limit. Since this did not yield the results obtained from direct simulations, we now include the dissipation terms and work with the Navier-Stokes equation.

The continuity equations of mass, momentum, and energy, after including the dissipation terms, in the radial coordinates are given by [1, 3, 27, 28],

$$\partial_t \rho + \partial_r(\rho u) + \frac{2\rho u}{r} = 0, \quad (43)$$

$$\partial_t(\rho u) + \partial_r(\rho u^2 + p) + \frac{2}{r}\rho u^2 = \frac{1}{r^2}\partial_r(2\mu r^2\partial_r u) - \frac{4\mu u}{r^2} + \partial_r \left[\left(\zeta - \frac{2}{3}\mu \right) \frac{1}{r^2}\partial_r(r^2 u) \right], \quad (44)$$

$$\begin{aligned} \partial_t \left[\frac{1}{2}\rho u^2 + \frac{1}{\gamma-1}\rho T \right] + \partial_r \left[\left(\frac{1}{2}\rho u^2 + \frac{1}{\gamma-1}\rho T + p \right) u \right] + \frac{2}{r}u \left[\frac{1}{2}\rho u^2 + \frac{1}{\gamma-1}\rho T + p \right] &= \frac{1}{r^2}\partial_r(2r^2\mu u\partial_r u) \\ + \frac{1}{r^2}\partial_r \left(u \left[\zeta - \frac{2}{3}\mu \right] \partial_r(r^2 u) \right) + \frac{1}{r^2}\partial_r(r^2\lambda\partial_r T) + \text{driving term}, \end{aligned} \quad (45)$$

where μ is the viscosity, λ is the heat conductivity, and ζ is the bulk viscosity.

The viscosity μ and heat conduction λ of a fluid of hard spheres increase with temperature $T(r, t)$ as [27, 29],

$$\mu = C_1\sqrt{T}, \quad (46)$$

$$\lambda = C_2\sqrt{T}, \quad (47)$$

where C_1 and C_2 are the coefficients of viscosity and heat conduction respectively. From kinetic theory of gases, the approximate values of C_1 and C_2 for hard sphere particles of diameter D , which we denote by C_1^* and C_2^* , are given by [29],

$$C_1^* = \frac{2}{3D^2}\sqrt{\frac{mk_B}{\pi^3}}, \quad (48)$$

$$C_2^* = \frac{1}{D^2}\sqrt{\frac{k_B^3}{m\pi^3}}, \quad (49)$$

where m is the mass of a particle, and k_B is Boltzmann constant. The bulk viscosity for mono-atomic gas is zero [30].

We use MacCormack method [31] to numerically solve the Navier-Stokes Eqs. (43)–(45), for $\delta = 1$. This method has accuracy up to second order both in time discretization Δt and radial discretization Δr . We call the numerical solution of NSE as direct numerical solution (DNS). The initial conditions on thermodynamic quantities at $t = 0$ are given by: constant density everywhere, zero velocity everywhere, and zero temperature everywhere. For the energy source at the origin, instead of taking a delta function energy source, we take it as a Gaussian to avoid numerical difficulties. We replace the driving term in Eq. (45) by

$$\text{driving term} = \frac{A_0}{4\pi r^2} \exp \left[\frac{-r^2 A_0^2 \pi}{4E_0^2} \right], \quad (50)$$

such that energy increases as $E_0 t$. To avoid edge effects, we choose system size L in such a manner that shock does not reach to the boundary upto the maximum time we integrate. We use boundary conditions where at the shock center, $r = 0$, the radial derivative of density and temperature are zero, and radial velocity is set to zero, and at the boundary of the region, the initial ambient values

TABLE III. The numerical values of different parameters used in solving the Navier-Stokes Eqs. (43)–(45).

Parameters	Values	Parameters	Values
δ	1.0	ρ_0	0.4013
Δr	0.08	Δt	10^{-5}
A_0	10^{-4}	L	300
γ	5/3	ζ	0
C_1^*	$2/(3\sqrt{\pi^3})$	C_2^*	$1/\sqrt{\pi^3}$

are maintained for each of the thermodynamic quantities [16]. The numerical values of the parameters that we use in our DNS are tabulated in the Table III.

We first benchmark the DNS using the same criteria that we used for EDMD, ie by validating the growth of total energy, radial momentum, and radius of shock front: $E(t) \sim t$, $M(t) \sim t^{7/5}$ [Eq. (33)], and $R(t) \sim t^{3/5}$ [Eq. (34)]. We first confirm that in the DNS, the total energy increases as $E_0 t$ as can be seen from Fig. 7(a). The DNS reproduce the power law growth for both shock radius as well as radial momentum for large times, as can be seen in Fig. 7(b) and (c).

Before comparing the DNS results with results from EDMD simulations, we first examine the role of the various parameters like EOS, dissipation coefficients on the data. We point out that we obtain data collapse of the data for different times when appropriately scaled [see Sec. IV]. For the dependence on parameters, we examine the data for one time.

In Fig. 8, we show the variation of non-dimensionalised thermodynamic functions [Eqs. (43)–(45)] with ξ for the virial EOS with the series truncated at the $i = 0, 2, 4, 6, 8, 10$ term. The results corresponding to $i = 0$ represent the DNS for ideal EOS. The data corresponding to $i = 8, 10$, lie on top of each other, thus showing negligible truncation error beyond the 10-th term. We will therefore work with virial EOS of 10 terms.

To study the role of viscosity, we study the DNS with five different values of coefficient of viscosity $C_1 = C_1^*/4, C_1^*/2, C_1^*, 2C_1^*, 4C_1^*$ keeping the heat conduction fixed at $C_2 = C_2^*$. We find that the value of C_1 does not affect the results much as can be seen from Fig. 9, where the different thermodynamics quantities are shown. We

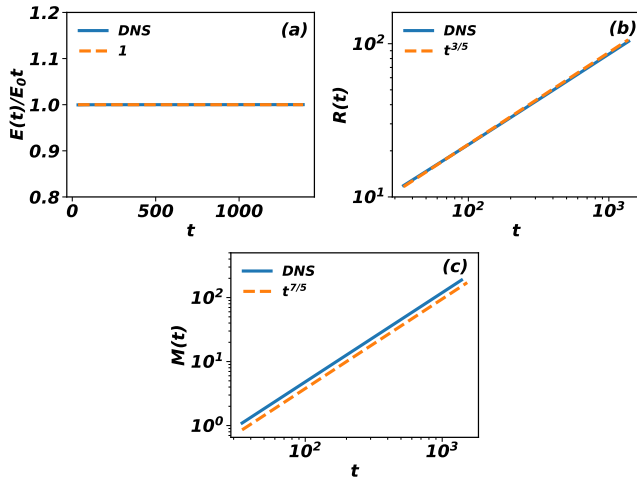


FIG. 7. Power law growth of (a) total energy $E(t) = E_0 t$, (b) radius of the shock front $R(t) \sim t^{3/5}$, and (c) total radial momentum $M(t) \sim t^{7/5}$ of the system. Solid lines represent the results from DNS, and dashed lines represent the respective power laws. The DNS data shown here are for ambient gas density $\rho_0 = 0.4013$, $A_0 = 10^{-4}$, $C_1 = C_1^*$, $C_2 = C_2^*$, and $\zeta = 0$.

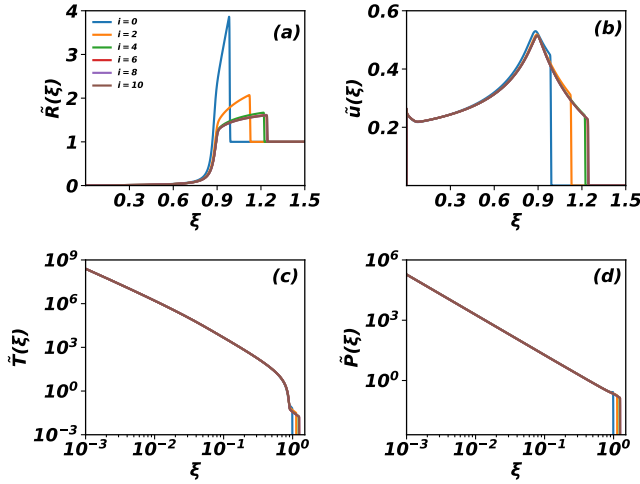


FIG. 8. The role of the EOS on the DNS data for (a) density $\tilde{R}(\xi)$, (b) velocity $\tilde{u}(\xi)$, (c) temperature $\tilde{T}(\xi)$, and (d) pressure $\tilde{P}(\xi)$. The virial EOS [see Eq. (35)] is truncated at $i = 0, 2, 4, 6, 8, 10$. The DNS data shown here are for initial density $\rho_0 = 0.4013$, $A_0 = 10^{-4}$, $C_1 = C_1^*$, $C_2 = C_2^*$, $\zeta = 0$, and time $t = 2t'_0$.

conclude that the DNS data are not sensitive to the value of the viscosity of the gas.

To study the role of heat dissipation, we study the DNS with five different values of coefficient of heat conductivity $C_2 = C_2^*/4, C_2^*/2, C_2^*, 2C_2^*, 4C_2^*$ keeping viscosity $C_1 = C_1^*$ fixed. Unlike the case of viscosity, we find that the different thermodynamic quantities, except pressure, depend on the value of C_2 , as can be seen from Fig. 10.

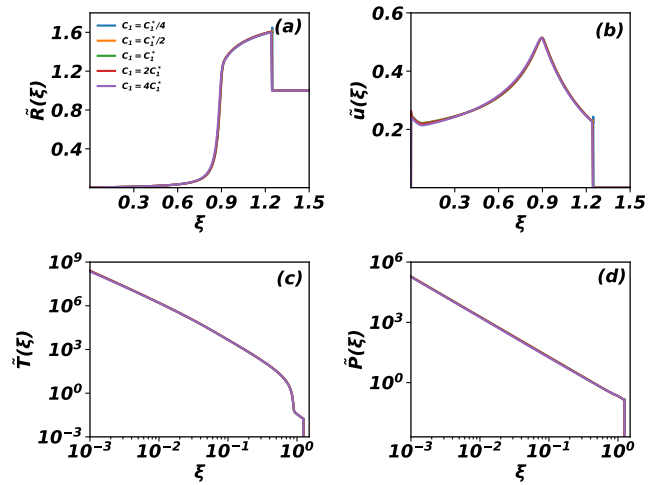


FIG. 9. The non-dimensionalised (a) density $\tilde{R}(\xi)$, (b) velocity $\tilde{u}(\xi)$, (c) temperature $\tilde{T}(\xi)$, and (d) pressure $\tilde{P}(\xi)$ obtained from the DNS of Eqs. (43)–(45) for five different values of coefficient of viscosity $C_1 = C_1^*/4, C_1^*/2, C_1^*, 2C_1^*, 4C_1^*$, keeping coefficient of heat conduction fixed at $C_2 = C_2^*$. The DNS data shown here are for initial density $\rho_0 = 0.4013$, $A_0 = 10^{-4}$, virial EOS up to 10^{th} terms, $\zeta = 0$, and time $t = 2t'_0$, where $t'_0 = 69.2$.

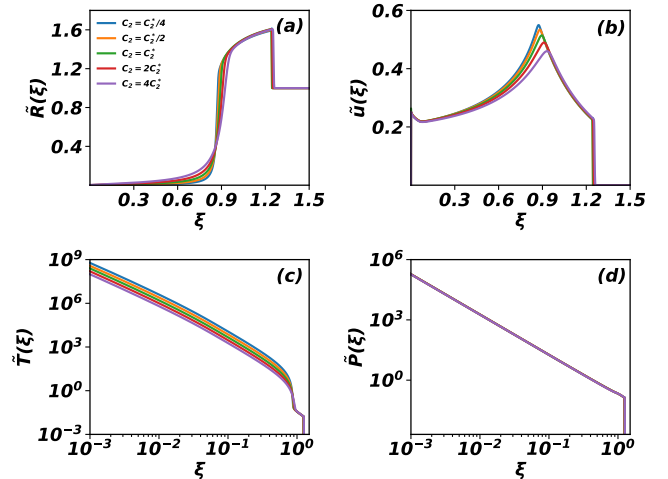


FIG. 10. The non-dimensionalised (a) density $\tilde{R}(\xi)$, (b) velocity $\tilde{u}(\xi)$, (c) temperature $\tilde{T}(\xi)$, and (d) pressure $\tilde{P}(\xi)$ obtained from the DNS of Eqs. (43)–(45) for five different values of coefficient of heat conduction $C_2 = C_2^*/4, C_2^*/2, C_2^*, 2C_2^*, 4C_2^*$, keeping coefficient of viscosity fixed at $C_1 = C_1^*$. The DNS data shown here are for initial density $\rho_0 = 0.4013$, $A_0 = 10^{-4}$, virial EOS up to 10^{th} terms, $\zeta = 0$, and time $t = 2t'_0$, where $t'_0 = 69.2$.

IV. COMPARISON BETWEEN THE EULER EQUATION, EDMD, AND DNS

We now compare the results from the different schemes that we have used to study continuous shock: simulations of discrete hard spheres using EDMD, solution of Euler

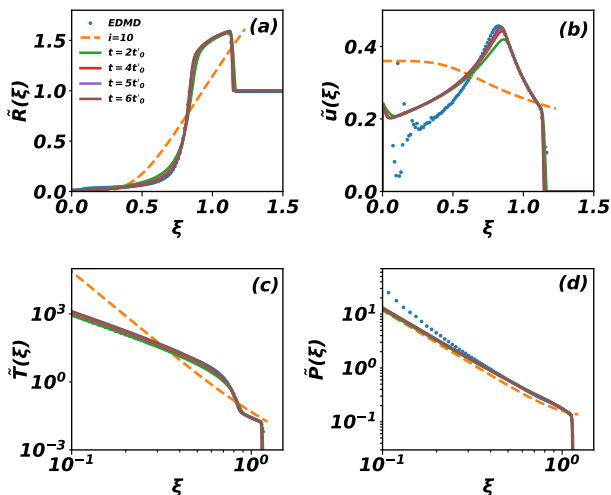


FIG. 11. The comparison between the profiles of non-dimensionalised (a) density $\tilde{R}(\xi)$, (b) velocity $\tilde{u}(\xi)$, (c) temperature $\tilde{T}(\xi)$, and (d) pressure $\tilde{P}(\xi)$ obtained from Euler Eqs. (39)–(37), EDMD, and the DNS of Navier-Stokes Eqs. (43)–(45). The symbols represent single time EDMD data at time $t = 3t_0$. The solid lines denote the results of DNS at four different times $t = 2t_0, 4t_0, 5t_0, 6t_0$ where $t_0 = 69.2$, and the dashed lines represent the results of Euler equation. The data shown here for DNS are for initial density $\rho_0 = 0.4013$, $A_0 = 10^{-4}$, virial EOS up to 10^{th} terms, $\zeta = 0$, $C_1 = 10C_1^*$, $C_2 = 8.35C_2^*$, and the data for EDMD are for ambient gas density $\rho_0 = 0.4013$, $E_0 = 2.5 \times 10^{-6}$, $R_0 = 15.0$, $\Delta t = 0.15$, and 4×10^7 number of hard sphere particles.

equation, and DNS of the Navier-Stokes equation. The different non-dimensionalised quantities for four different times are shown in Fig. 11. To match with the EDMD data, we have run the DNS for different values of C_1 and C_2 , and chosen values with the best match. To do so, we started with the initial values of C_1 , and C_2 as C_1^* , and C_2^* respectively and then we increased these values systematically till we obtained a best fit (visually) to the data for all the scaling.

We first note the results of DNS for different times collapse onto a single curve verifying the scaling Eqs. (11)–(15). The DNS data is able to capture the EDMD data for $\tilde{R}(\xi)$, $\tilde{T}(\xi)$, and $\tilde{P}(\xi)$. However, there is slight discrepancy for the velocity field $\tilde{u}(\xi)$. Near the shock center, a quantitative mismatch between EDMD and DNS can be seen in the Fig. 11. A possible reason for this mismatch could be the different nature of driving in EDMD, and the appearance of the driving scale R_0 which could result in crossovers in the the data near the shock center.

V. SUMMARY AND DISCUSSION

In summary, we studied the hydrodynamics of shocks in a gas in which energy is continuously input at one localized region in space. Different schemes were used to study this problem: EDMD simulations, DNS of Navier-Stokes equation, and numerical solution of the Euler equation. We showed that the solution of Euler equation does not match with the EDMD data anywhere, but the numerical solution of Navier-Stokes equation shows a reasonable agreement with the EDMD results, provided the heat conduction and viscosity are chosen parametrically. We also showed that the different scaling functions \tilde{R} , \tilde{T} , and \tilde{P} , within the Euler equation, follow power law behavior close to the shock center with respective exponents are independent of the driving exponent δ . We conclude that even though the continuous drive takes the system far from equilibrium, Navier-Stokes equation continues to give a good description of the system.

The reason why Euler equation does not provide a good hydrodynamic description remains the same as that for the single impact. Temperature diverges at the shock center, within the Euler equation. Adding a heat conduction term regularizes this behavior with the radial derivative going to zero. This is what is observed in EDMD simulations also. Thus, the solution of the Euler equation does not respect the boundary conditions seen in simulations, leading to an incorrect description.

Incorporating heat conduction in the continuity equations altered the scaling near the shock center for the case of single impact. This crossover has been quantified in earlier work [19–21]. Generalizing these results to the case of driven shock is an interesting problem for future research. However, obtaining clean data near the shock center is a more challenging problem for driven shocks. Driving introduces a new length scale, defined by the region of driving, and hence taking the $r \rightarrow 0$ limit requires simulations of much larger systems.

Shock propagation has also been studied in granular systems where collisions between particles are inelastic. The creation of a shock due to a single impact is relevant for the study of crater formation due to the impact of particles having a high initial energy [32], dropping a steel ball vertically into a container of small glass beads [33], or due to the single impact of steel ball on flowing glass beads [34], and has been studied using scaling and simulations particle based models [14, 35]. For studying such shocks, the the TvNS theory has been modified for dissipative systems [18, 36]. Shocks due to continuous driving are also relevant for granular systems. For example, granular fingering or pattern formation due to continuous injection of a viscous liquid in dry dense granular medium [37–41], impinging of gas jets vertically on a granular bed [42] create outwardly moving disturbances and have been studied using scaling and particle based models [43]. Generalizing the theory [18, 36] to continuous driving, and checking its validity with experiments and simulation is a promising area of future research.

Appendix A: Review of exact solution of Euler equation

In this Appendix, we provide the analytical solution of ordinary differential Eqs. (17)–(19) satisfying the Rankine-Hugoniot boundary conditions (see Eqs. (20)–(22)) for non-dimensionalised scaling functions \tilde{R} , \tilde{u} , \tilde{T} , and \tilde{P} as defined in Eqs. (11)–(15). On further simplifying the Eqs. (17)–(19) for $d \log \xi / d\tilde{u}$ and $d \log \tilde{R} / d \log \xi$, we obtain

$$\frac{d\tilde{u}}{d \log \xi} = \frac{\tilde{u}(\gamma\tilde{u} - \alpha)[10\alpha^2 + 2\tilde{u}[(2 + \delta)(\tilde{u} - 2\alpha) + \gamma\alpha(\delta - 3)] + 3\tilde{u}^2(2 + \delta)(\gamma - 1)]}{(2 + \delta)[2\alpha^3 - 2\alpha\tilde{u}(\gamma + 2) + \alpha\tilde{u}^2(3 + 2\gamma + \gamma^2) - 2\gamma\tilde{u}^3 - \tilde{u}^2(\gamma - 1)(\gamma\tilde{u} - \alpha)]}, \quad (\text{A1})$$

$$\frac{d \log \tilde{R}}{d \log \xi} = \frac{3\tilde{u}(2 + \delta)[2\alpha^3 - 2\alpha^2\tilde{u}(\gamma + 2) + \alpha\tilde{u}^2(3 + 2\gamma + \gamma^2) - 2\gamma\tilde{u}^3] + 2\tilde{u}(\gamma\tilde{u} - \alpha)[5\alpha^2 + \tilde{u}[(2 + \delta)(\tilde{u} - 2\alpha) + \alpha\gamma(\delta - 3)]]}{(2 + \delta)(\alpha - \tilde{u})[2\alpha^3 - 2\alpha^2\tilde{u}(\gamma + 2) + \alpha\tilde{u}^2(3 + 2\gamma + \gamma^2) - 2\gamma\tilde{u}^3 - \tilde{u}^2(\gamma - 1)(\gamma\tilde{u} - \alpha)]}, \quad (\text{A2})$$

$$\tilde{T} = \frac{\tilde{u}^2(\alpha - \tilde{u})(\gamma - 1)}{2(\gamma\tilde{u} - \alpha)}. \quad (\text{A3})$$

The above ordinary differential equations can be solved analytically. The solution depends on the sign of the parameter $a_1 = (\gamma - 2)^2(\delta^2 + 9) - (6\gamma^2 + 26\gamma - 26)\delta$. When $a_1 \geq 0$, we find

$$\tilde{R}(\tilde{u}) = \frac{\alpha b_1}{\alpha - \tilde{u}} (f_2(\tilde{u}))^{a_8} \left(\frac{\gamma\tilde{u} - \alpha}{\alpha(\gamma - 1)} \right)^{a_9} \exp \left(\frac{a_7}{\sqrt{a_1}} \left[\tanh^{-1} \left(\frac{f_1(\tilde{u})}{\sqrt{a_1}} \right) - \tanh^{-1} \left(\frac{a_5}{\sqrt{a_1}} \right) \right] \right), \quad (\text{A4})$$

$$\left(\frac{10}{2 + \delta} \right) \log \left(\frac{\xi(\tilde{u})}{\xi_f} \right) = \frac{a_2}{\sqrt{a_1}} \left[\tanh^{-1} \left(\frac{a_5}{\sqrt{a_1}} \right) - \tanh^{-1} \left(\frac{f_1(\tilde{u})}{\sqrt{a_1}} \right) \right] + a_3 \log \left(\frac{\gamma\tilde{u} - \alpha}{\alpha(\gamma - 1)} \right) + \log \left(\frac{(\alpha^2 f_2(\tilde{u}))^{a_4}}{\tilde{u}^2} \right) + b_2. \quad (\text{A5})$$

On the other hand, when $a_1 < 0$, we obtain

$$\tilde{R}(\tilde{u}) = \frac{\alpha b_1}{\alpha - \tilde{u}} (f_2(\tilde{u}))^{a_8} \left(\frac{\gamma\tilde{u} - \alpha}{\alpha(\gamma - 1)} \right)^{a_9} \exp \left(\frac{a_7}{\sqrt{-a_1}} \left[\tan^{-1} \left(\frac{a_5}{\sqrt{-a_1}} \right) - \tan^{-1} \left(\frac{f_1(\tilde{u})}{\sqrt{-a_1}} \right) \right] \right), \quad (\text{A6})$$

$$\left(\frac{10}{2 + \delta} \right) \log \left(\frac{\xi(\tilde{u})}{\xi_f} \right) = \frac{a_2}{\sqrt{-a_1}} \left[\tan^{-1} \left(\frac{f_1(\tilde{u})}{\sqrt{-a_1}} \right) - \tan^{-1} \left(\frac{a_5}{\sqrt{-a_1}} \right) \right] + a_3 \log \left(\frac{\gamma\tilde{u} - \alpha}{\alpha(\gamma - 1)} \right) + \log \left(\frac{(\alpha^2 f_2(\tilde{u}))^{a_4}}{\tilde{u}^2} \right) + b_2, \quad (\text{A7})$$

where,

$$a_2 = \frac{2((6\gamma^3 - 11\gamma^2 - 3\gamma + 2)\delta^2 + (19\gamma^3 + 16\gamma^2 + 33\gamma - 32)\delta + 39\gamma^3 - 99\gamma^2 + 78\gamma - 72)}{(2\gamma + 1)(3\gamma - 1)(\delta + 2)}, \quad (\text{A8})$$

$$a_3 = \frac{10(\gamma - 1)}{(2\gamma + 1)(\delta + 2)}, \quad (\text{A9})$$

$$a_4 = \frac{(6\gamma^2 + \gamma - 1)\delta - 13\gamma^2 + 7\gamma - 12}{(2\gamma + 1)(3\gamma - 1)(\delta + 2)}, \quad (\text{A10})$$

$$a_5 = \frac{(\gamma^2 + 5\gamma - 4)\delta - 3\gamma^2 + 5\gamma - 8}{\gamma + 1}, \quad (\text{A11})$$

$$a_6 = \frac{2((2\gamma^2 + 4\gamma - 6)\delta - \gamma^2 + 8\gamma - 7)}{(\gamma + 1)^2}, \quad (\text{A12})$$

$$a_7 = \frac{6(\gamma + 3)((\gamma^2 + \gamma - 1)\delta - 3\gamma^2 + 2\gamma - 2)}{(6\gamma^2 + \gamma - 1)}, \quad (\text{A13})$$

$$a_8 = \frac{3(\gamma^2 + 1)}{6\gamma^2 + \gamma - 1}, \quad (\text{A14})$$

$$a_9 = \frac{3}{2\gamma + 1}, \quad (\text{A15})$$

$$b_1 = (\gamma + 1)^{a_9} a_6^{-a_8}, \quad (\text{A16})$$

$$b_2 = a_3 \log(\gamma + 1) - a_4 \log(a_6) + 2 \log\left(\frac{2}{\gamma + 1}\right), \quad (\text{A17})$$

$$f_1(\tilde{u}) = (3\gamma - 1)(\delta + 2)\tilde{u}/\alpha + (\gamma - 2)\delta - 3\gamma - 4, \quad (\text{A18})$$

$$f_2(\tilde{u}) = (3\gamma - 1)(\delta + 2)\tilde{u}^2/\alpha^2 + 2((\gamma - 2)\delta - 3\gamma - 4)\tilde{u}/\alpha + 10. \quad (\text{A19})$$

We have checked for the correctness of the solution by checking that they match with the numerical solution of the differential equations.

The value of ξ_f can be obtained by using the energy constraint $E(t) = E_0 t^\delta$ [see Eq. (23)]. The analytical solutions show the following asymptotic behavior of scaling functions, as $\xi \rightarrow 0$,

$$\tilde{u} - \frac{\alpha}{\gamma} \rightarrow \xi^{\frac{2\gamma+1}{\gamma-1}} \quad (\text{A20})$$

$$\tilde{R} \rightarrow \xi^{\frac{3}{\gamma-1}} \quad (\text{A21})$$

$$\tilde{T} \rightarrow \xi^{-\frac{2\gamma+1}{\gamma-1}}. \quad (\text{A22})$$

-
- [1] L. D. Landau and E. M. Lifshitz, *Fluid Mechanics*, Course of theoretical physics, Vol. 6 (Butterworth-Heinemann, Oxford UK, 1987).
- [2] G. I. Barenblatt, *Scaling, self-similarity, and intermediate asymptotics: dimensional analysis and intermediate asymptotics* (Cambridge University Press, 1996).
- [3] G. B. Whitham, *Linear and nonlinear waves* (John Wiley & Sons, 2011).
- [4] G. I. Taylor, The formation of a blast wave by a very intense explosion i. theoretical discussion, Proc. Roy. Soc. A **201**, 159 (1950).
- [5] G. I. Taylor, The formation of a blast wave by a very intense explosion.-ii. the atomic explosion of 1945, Proc. Roy. Soc. A **201**, 175 (1950).
- [6] J. von Neumann, in *Collected Works* (Pergamon Press, Oxford, 1963) p. 219.
- [7] L. Sedov, *Similarity and Dimensional Methods in Mechanics*, 10th ed. (CRC Press, Florida, 1993).
- [8] L. Sedov, J. Appl. Math. Mech. **10**, 241 (1946).
- [9] V. Dokuchaev, Self-similar spherical shock solution with sustained energy injection, Astronomy & Astrophysics **395**, 1023 (2002).
- [10] K. P. Stanyukovich, *Unsteady motion of continuous media* (Elsevier, 2016).
- [11] M. Edwards, A. MacKinnon, J. Zweiback, K. Shigemori, D. Ryutov, A. Rubenchik, K. Keilty, E. Liang, B. Remington, and T. Ditmire, Investigation of ultrafast laser-driven radiative blast waves, Phys. Rev. Lett. **87**, 085004

- (2001).
- [12] A. Edens, T. Ditmire, J. Hansen, M. Edwards, R. Adams, P. Rambo, L. Ruggles, I. Smith, and J. Porter, Study of high mach number laser driven blast waves, *Phys. Plasma* **11**, 4968 (2004).
- [13] A. S. Moore, D. R. Symes, and R. A. Smith, Tailored blast wave formation: Developing experiments pertinent to laboratory astrophysics, *Phys. Plasma* **12**, 052707 (2005).
- [14] Z. Jabeen, R. Rajesh, and P. Ray, Universal scaling dynamics in a perturbed granular gas, *EPL (Europhysics Letters)* **89**, 34001 (2010).
- [15] J. P. Joy, S. N. Pathak, and R. Rajesh, Shock propagation following an intense explosion: comparison between hydrodynamics and simulations, *J. Stat. Phys.* **182**, 1 (2021).
- [16] A. Kumar and R. Rajesh, Blast waves in two and three dimensions: Euler versus navier–stokes equations, *Journal of Statistical Physics* **188**, 1 (2022).
- [17] J. P. Joy and R. Rajesh, Shock propagation in the hard sphere gas in two dimensions: comparison between simulations and hydrodynamics, *J. Stat. Phys.* **184**, 1 (2021).
- [18] M. Barbier, D. Villamaina, and E. Trizac, Microscopic origin of self-similarity in granular blast waves, *Phys. Fluids* **28**, 083302 (2016).
- [19] S. Ganapa, S. Chakraborti, P. Krapivsky, and A. Dhar, Blast in the one-dimensional cold gas: Comparison of microscopic simulations with hydrodynamic predictions, *Phys. Fluids* **33**, 087113 (2021).
- [20] S. Chakraborti, S. Ganapa, P. Krapivsky, and A. Dhar, Blast in a one-dimensional cold gas: From newtonian dynamics to hydrodynamics, *Phys. Rev. Lett.* **126**, 244503 (2021).
- [21] S. K. Singh, S. Chakraborti, A. Dhar, and P. Krapivsky, Blast waves in the zero temperature hard sphere gas: double scaling structure, *Journal of Statistical Physics* **190**, 118 (2023).
- [22] V. Avedisova, Formation of nebulae by wolf-rayet stars., *Soviet Astronomy* **15**, 708 (1972).
- [23] S. Falle, A numerical calculation of the effect of stellar winds on the interstellar medium, *Astronomy and Astrophysics* **43**, 323 (1975).
- [24] D. C. Rapaport and D. C. R. Rapaport, *The art of molecular dynamics simulation* (Cambridge university press, 2004).
- [25] M. Isobe, Hard sphere simulation in statistical physics—methodologies and applications, *Molecular Simulation* **42**, 1317 (2016).
- [26] B. M. McCoy, *Advanced statistical mechanics*, Vol. 146 (Oxford University Press, 2010).
- [27] K. Huang, *Statistical mechanics*, john wily & sons, New York , 10 (1963).
- [28] Z. U. Warsi, *Fluid dynamics: theoretical and computational approaches* (CRC press, 2005).
- [29] F. Reif, *Fundamentals of statistical and thermal physics* (Waveland Press, 2009).
- [30] R. Boukharfane, P. J. M. Ferrer, A. Mura, and V. Giovangigli, On the role of bulk viscosity in compressible reactive shear layer developments, *European Journal of Mechanics-B/Fluids* **77**, 32 (2019).
- [31] R. W. MacCormack, A numerical method for solving the equations of compressible viscous flow, *AIAA journal* **20**, 1275 (1982).
- [32] Y. Grasselli and H. Herrmann, Crater formation on a three dimensional granular heap, *Granular Matter* **3**, 201 (2001).
- [33] A. M. Walsh, K. E. Holloway, P. Habdas, and J. R. de Bruyn, Morphology and scaling of impact craters in granular media, *Phys. Rev. Lett.* **91**, 104301 (2003).
- [34] J.-F. Boudet, J. Cassagne, and H. Kellay, Blast shocks in quasi-two-dimensional supersonic granular flows, *Phys. Rev. Lett.* **103**, 224501 (2009).
- [35] S. N. Pathak, Z. Jabeen, P. Ray, and R. Rajesh, Shock propagation in granular flow subjected to an external impact, *Phys. Rev. E* **85**, 061301 (2012).
- [36] M. Barbier, D. Villamaina, and E. Trizac, Blast dynamics in a dissipative gas, *Phys. Rev. Lett.* **115**, 214301 (2015).
- [37] X. Cheng, L. Xu, A. Patterson, H. M. Jaeger, and S. R. Nagel, Towards the zero-surface-tension limit in granular fingering instability, *Nature Physics* **4**, 234 (2008).
- [38] B. Sandnes, H. Knudsen, K. Måløy, and E. Flekkøy, Labyrinth patterns in confined granular-fluid systems, *Phys. Rev. Lett.* **99**, 038001 (2007).
- [39] S. Pinto, M. Couto, A. Atman, S. Alves, A. T. Bernardes, H. de Resende, and E. Souza, Granular fingers on jammed systems: New fluidlike patterns arising in grain-grain invasion experiments, *Phys. Rev. Lett.* **99**, 068001 (2007).
- [40] Ø. Johnsen, R. Toussaint, K. J. Måløy, and E. G. Flekkøy, Pattern formation during air injection into granular materials confined in a circular hele-shaw cell, *Phys. Rev. E* **74**, 011301 (2006).
- [41] H. Huang, F. Zhang, P. Callahan, and J. Ayoub, Granular fingering in fluid injection into dense granular media in a hele-shaw cell, *Phys. Rev. Lett.* **108**, 258001 (2012).
- [42] P. T. Metzger, R. C. Latta III, J. M. Schuler, and C. D. Immer, Craters formed in granular beds by impinging jets of gas, in *AIP Conference Proceedings*, Vol. 1145 (American Institute of Physics, 2009) pp. 767–770.
- [43] J. P. Joy, S. N. Pathak, D. Das, and R. Rajesh, Shock propagation in locally driven granular systems, *Phys. Rev. E* **96**, 032908 (2017).